Strain-induced seismic anisotropy of wadsleyite polycrystals and flow patterns in the mantle transition zone

Andréa Tommasi,[1] David Mainprice,[1] Patrick Cordier,[2] Catherine Thoraval,[1] and Hélène Couvy[2,3]

Received 29 April 2004; revised 4 October 2004; accepted 8 October 2004; published 17 December 2004.

[1] We use forward models based on recent high-pressure experimental data on mantle minerals to predict the seismic anisotropy produced by plastic strain of orthorhombic wadsleyite, the dominant mineral in the upper transition zone. These models predict a weak seismic anisotropy for a polycrystal of pyrolitic composition (60% wadsleyite, 40% garnet) at transition zone conditions: ~2% for *P* and ~1% for *S* waves for a shear strain of 1. Both *P* and *S* wave anisotropy patterns show an orthorhombic symmetry. *P* waves propagate faster at low angle to the shear direction and slower at high angle to the shear plane. *S* wave anisotropy is characterized by faster propagation of waves polarized at low angle to the shear direction. Horizontal shearing results therefore in higher velocities for horizontally propagating *P* waves (*PH*) and horizontally polarized *S* waves (*SH*), as well as in weak azimuthal variation of *SV* and *SH* velocities. On the other hand, vertical flow leads to higher velocities for vertically propagating *P* waves (*PV*) and vertically polarized *S* waves (*SV*) and to a weak azimuthal variation of *SV* velocity but to a roughly constant *SH* velocity. Analysis of global observations of seismic anisotropy in the transition zone in the light of these models supports dominant horizontal flow in the uppermost transition zone, in agreement with predictions of geodynamical models that explicitly introduce phase transitions. *INDEX TERMS:* 3902 Mineral Physics: Creep and deformation; 8120 Tectonophysics: Dynamics of lithosphere and mantle—general; 8121 Tectonophysics: Dynamics, convection currents and mantle plumes; 7207 Seismology: Core and mantle; *KEYWORDS:* mantle convection, seismic anisotropy, crystal preferred orientation

Citation: Tommasi, A., D. Mainprice, P. Cordier, C. Thoraval, and H. Couvy (2004), Strain-induced seismic anisotropy of wadsleyite polycrystals and flow patterns in the mantle transition zone, *J. Geophys. Res.*, *109*, B12405, doi:10.1029/2004JB003158.

1. Introduction

[2] Convection patterns in the Earth's mantle depend strongly on how physical properties are modified by the pressure-induced phase changes that take place in the transition zone, i.e., between 410 and 670 km depth. After a long debate on whether mantle convection was double- or single-layered, current models tend to favor a single-layer convection in which the transition zone behaves as a more or less permeable barrier. Indeed, geodynamical models show that, because of its negative Clapeyron slope [*Akaogi et al.*, 1989], the ringwoodite to perovskite + magnesiowustite phase change at the base of the transition zone slows material transfer across the transition zone, leading to intermittently layered convection [*Christensen and Yuen*, 1985; *Machetel and Weber*, 1991]. This convection style, in between whole mantle and layered convection, may explain, for instance, that some slabs, like the Marianas and Java, plunge steeply across the transition zone, penetrating promptly into the lower mantle, whereas others, like the Japan, southern Kurile, and Izu-Bonin, are deflected within the transition zone [*van der Hilst et al.*, 1991]. Partially (or locally) layered convection also reconciles dynamic topography predicted in mantle circulation models with observations [*Thoraval et al.*, 1995; *Cadek and Fleitout*, 1999].

[3] Knowledge of flow patterns within the transition zone layer is thus essential to constrain the structure of mantle circulation. Seismic anisotropy observations are undoubtedly the best tool to image flow patterns in the deep Earth, since anisotropy, as in the upper mantle, may result from strain-induced crystal-preferred orientation (CPO) of elastically anisotropic minerals. Seismic anisotropy in the transition zone at a global scale was first suggested by a joint analysis of body wave travel times and free oscillation frequencies [*Montagner and Kennett*, 1996], which showed that these data may be reconciled by a weak radial anisotropy in the transition zone. This anisotropy is characterized by higher velocities of horizontally propagating compressional waves (*PH*) and horizontally polarized shear waves (*SH*) relatively to vertically propagating compressional waves (*PV*) and vertically polarized shear waves (*SV*), respectively. Faster

[1] Laboratoire de Tectonophysique, CNRS/Université de Montpellier II, Montpellier, France.
[2] Laboratoire Structure et Propriétés de l'Etat Solide, CNRS/Université de Lille, Villeneuve d'Ascq, France.
[3] Bayerisches Geoinstitut, Universität Bayreuth, Bayreuth, Germany.

0148-0227/04/2004JB003158$09.00

propagation of *SH* waves in the transition zone beneath oceans is also suggested by probability density functions for radial anisotropy obtained from Love and Rayleigh phase velocity models [*Beghein and Trampert*, 2004]. In contrast, these data suggest that *PV* waves tend to propagate faster than *PH* beneath tectonically active regions. Additional evidence for an anisotropic transition zone comes from global surface wave dispersion measurements for Love wave overtones that imply azimuthal anisotropy for both vertically and horizontally polarized shear waves in the transition zone, the former displaying a higher anisotropy (up to 2%) than the latter [*Trampert and van Heijst*, 2002].

[4] Anisotropy in the transition zone is also evidenced by regional studies that analyze the polarization anisotropy of shear waves turning within the transition zone beneath northern Australia and within the northern Tonga subduction [*Tong et al.*, 1994; *Chen and Brudzinski*, 2003]. Both data sets show horizontally polarized shear waves (*SH*) arriving 2–3 s earlier than vertically polarized shear waves (*SV*). In contrast, comparison between *SKS* and local *S* splitting data beneath various North Pacific subduction zones shows that vertically propagating shear waves generally do not detect seismic anisotropy in the transition zone, except for weak anisotropy in the 410–520 km depth range beneath the South Kurils [*Fouch and Fischer*, 1996]. Finally, azimuthal anisotropy in the deep transition zone beneath Eurasia is also suggested by analysis of compressional to shear wave conversions [*Vinnik and Montagner*, 1996].

[5] Within the volumetrically important mineral phases in the transition zone (wadsleyite, ringwoodite, and garnet), wadsleyite, which is the dominant mineral phase between 410 and 520 km depth, displays the strongest intrinsic elastic anisotropy [*Mainprice et al.*, 2000]. At transition zone pressures, the wadsleyite crystal shows 11–13% propagation anisotropy for shear waves and compressional waves, respectively [*Zha et al.*, 1997; *Sinogeikin et al.*, 1998]. However, seismic anisotropy will only be observed if deformation in the transition zone leads to the development of coherent crystal preferred orientations of wadsleyite at the length scales sampled by seismic waves, i.e., at least several hundreds of kilometers for surface waves. Moreover, crystal preferred orientations may result in a large-scale seismic anisotropy pattern that significantly differs from the single-crystal one. Finally, layered structures or oriented inclusions of materials with contrasting elastic properties may also produce seismic anisotropy. Deduction of flow patterns from seismic anisotropy data is therefore not straightforward.

[6] For the upper mantle, forward modeling of development of crystal preferred orientations and seismic anisotropy in response to a given flow process has proven successful in constraining the interpretation of seismological observations in terms of mantle deformation [*Ribe*, 1989; *Chastel et al.*, 1993; *Blackman et al.*, 1996; *Tommasi*, 1998; *Tommasi et al.*, 1999; *Kaminski and Ribe*, 2002]. This approach can now be used to unravel flow patterns in the deep mantle. Recent technological developments allow deformation experiments on mantle materials to be performed at transition zone temperature and pressure conditions [*Bussod et al.*, 1993; *Cordier and Rubie*, 2001; *Durham et al.*, 2002]. These experiments provide essential information on flow mechanisms of the transition zone and lower mantle mineral phases. Transmission electron microscopy on wadsleyite polycrystals deformed in compression and simple shear in multianvil apparatus showed dislocations in glide configuration as well as subgrains, suggesting deformation by dislocation creep [*Dupas et al.*, 1994; *Sharp et al.*, 1994; *Dupas-Bruzek et al.*, 1998; *Thurel and Cordier*, 2003; *Thurel et al.*, 2003a]. Early experiments, which associated olivine to wadsleyite transformation under nonhydrostatic stress and deformation, suggested that wadsleyite may deform by glide on [100](010), [100]{021}, and 1/2⟨111⟩ systems [*Dupas et al.*, 1994; *Sharp et al.*, 1994; *Dupas-Bruzek et al.*, 1998]. A recent extensive large angle convergent beam electron diffraction (LACBED) analysis of dislocation structures on wadsleyite polycrystals deformed at 14 GPa and 1300°C improved the determination of the active slip systems [*Thurel et al.*, 2003b]; under transition zone conditions wadsleyite deforms mainly by slip on [100]{0kl} and 1/2⟨111⟩{101} systems (Figure 1). On the basis of these data, we use polycrystal plasticity simulations to predict the evolution of crystal preferred orientations (CPO) as a function of strain and then evaluate the strain-induced seismic anisotropy in the upper transition zone.

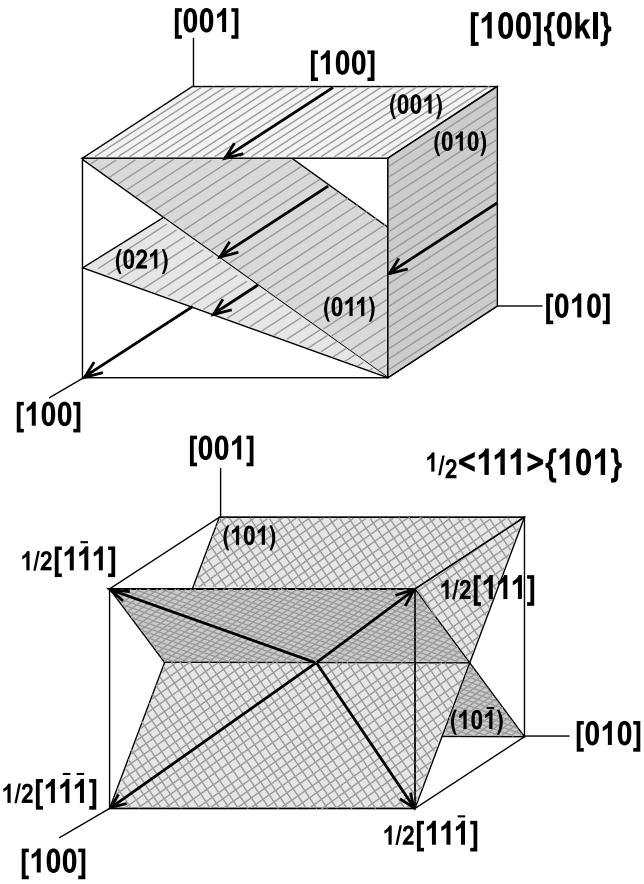

Figure 1. Slip systems in the wadsleyite crystal.

2. Strain-Induced Wadsleyite Crystal Preferred Orientations

[7] Development of crystal preferred orientations (CPO) in wadsleyite polycrystals is simulated using a viscoplastic

self-consistent (VPSC) model [*Lebensohn and Tomé*, 1993]. In this model, as in all polycrystal plasticity approaches, CPO evolution is essentially controlled by the imposed deformation, the initial texture (crystal preferred and, to a lesser extent, shape preferred orientation), and the active slip systems. The latter depend on the mineral structure, but also on the temperature and pressure conditions, which control their relative strength or critical resolved shear stress (CRSS). Extensive testing on metallic alloys [*Lebensohn and Tomé*, 1993; *Logé et al.*, 2000], halite [*Lebensohn et al.*, 2003], as well as on highly anisotropic minerals, such as calcite [*Tomé et al.*, 1991], olivine [*Wenk et al.*, 1991; *Tommasi et al.*, 2000], and clinopyroxene [*Bascou et al.*, 2002], shows that this model produces robust CPO predictions.

[8] In contrast to classical lower or upper bound approaches, which impose respectively homogeneous stress [*Sachs*, 1928] or strain [*Taylor*, 1938] within the aggregate, the VPSC approach allows both the microscopic stress and strain rate to differ from the corresponding macroscopic quantities. Strain compatibility and stress equilibrium are ensured only at the aggregate scale. At the grain scale, deformation is homogeneous. It is accommodated by dislocation glide only. The shear rate in a slip system s is related to the local deviatoric stress tensor $\mathbf{s}$ by a viscoplastic law:

$$\dot{\gamma}^s = \dot{\gamma}_0 \left(\frac{\tau_r^s}{\tau_0^s} \right) = \dot{\gamma}_0 \left(\frac{r_{ij}^s s_{ij}}{\tau_0^s} \right)^{n^s}, \tag{1}$$

where $\dot{\gamma}_0$ is a reference strain rate, taken as 1 s^{-1}, and n^s, τ_r^s, and τ_0^s are respectively the stress exponent, the resolved shear stress, and the CRSS for the system s, whose orientation relative to the macroscopic axis is expressed by its Schmid tensor $\mathbf{r}^s$.

[9] The problem lies in the calculation of a microscopic state ($\mathbf{s}$, $\dot{\varepsilon}$) for each grain, whose volume average determines the response of the polycrystal ($\bar{\Sigma}$, $\bar{\mathbf{D}}$). The "one-site" approximation [*Molinari et al.*, 1987; *Lebensohn and Tomé*, 1993] is used in the anisotropic VPSC formulation; interactions between neighboring grains are hence not taken into account. Interactions between each grain and its surroundings are replaced by the interaction between an inclusion with the same lattice orientation and an infinite homogeneous equivalent medium (HEM), whose behavior is the volume weighted average of the grain's behavior. This leads to:

$$\dot{\varepsilon}_{ij} - D_{ij} = -\alpha M_{ijkl}(S_{kl} - \Sigma_{kl}), \tag{2}$$

where $\tilde{\mathbf{M}}$ is the interaction tensor and α is a constant used to parameterize the interaction between grains and the HEM; $\alpha = 0$ corresponds to the upper bound model (homogeneous strain), $\alpha = 1$ is the classical self-consistent model, used in the present simulations (linear relationship between volume averaged stress and strain rate), and α = infinity corresponds to the lower bound model (stress equilibrium).

[10] In the present study, we investigate the evolution of wadsleyite CPO for an end-member deformation regime: simple shear. Actual flow in the transition zone is most likely three-dimensional, but regions submitted to large deformations probably display a strong shear component, whose orientation (horizontal or steeply dipping) will depend on the large-scale convection pattern. We also performed simulations in transpression (transtension), in which we add a weak compression (extension) normal to the shear plane, in axial compression, and in axial extension to evaluate the effect of a three-dimensional deformation on the CPO evolution and on the resulting seismic anisotropy. The strain history is imposed by prescribing a constant macroscopic velocity gradient tensor $\mathbf{L}$, which for simple shear is

$$\mathbf{L} = \begin{bmatrix} 0 & 1 & 0 \\ 0 & 0 & 0 \\ 0 & 0 & 0 \end{bmatrix}, \tag{3}$$

and a time increment, dt, set to achieve an equivalent strain of 0.025 in each deformation step. The equivalent strain is defined as

$$\varepsilon_{eq} = \int \mathbf{D}_{eq}(t) dt, \tag{4}$$

where the Von Mises equivalent strain rate is:

$$D_{eq} = \sqrt{2/3 D_{ij} D_{ij}}. \tag{5}$$

[11] The only tuning parameters are the active slip systems for wadsleyite, their CRSS and stress exponent. Active slip systems in wadsleyite at transition zone conditions are constrained by TEM observations on polycrystalline specimens deformed in the multianvil apparatus [*Thurel et al.*, 2003b]. These observations point to dominant glide on [100](010), [100](001), [100]{011}, [100]{021}, and $1/2\langle 111 \rangle \{101\}$ slip systems. There is no mechanical data on wadsleyite single crystals that would provide constraints on the relative strength of these slip systems (CRSS). However, TEM observations of similar densities of [100] and $1/2\langle 111 \rangle$ dislocations suggest that $1/2\langle 111 \rangle$ and [100] systems must have similar activities [*Thurel et al.*, 2003b]. We have therefore varied the relative CRSS for $1/2\langle 111 \rangle$ and [100] slip systems with a maximum ratio of 1:5 (or 5:1). Since the actual stress exponent for wadsleyite is unknown, we a used standard value for dislocation creep, n = 3, in all simulations. VPSC simulations are not very sensitive to n values between 3 and 5; the main effect of increasing n is an enhancement of the CPO for a given finite strain.

[12] Figure 2 shows CPO predicted for an aggregate of initially spherical and randomly oriented 500 wadsleyite grains after a shear strain of 1 by models with various CRSS values. As observed in previous VPSC models for olivine, clinopyroxene, and garnet [*Tommasi et al.*, 2000; *Bascou et al.*, 2002; *Mainprice et al.*, 2004], crystal preferred orientation predictions are robust features that depend weakly on the relative values of CRSS for individual slip systems. In most models, [100] axes tend to concentrate close to the shear direction and [001] axes are distributed in a girdle at high angle to the shear direction, with a clear maximum at 65° clockwise from the shear plane. This obliquity of the [001] maximum relative to the shear plane agrees with the

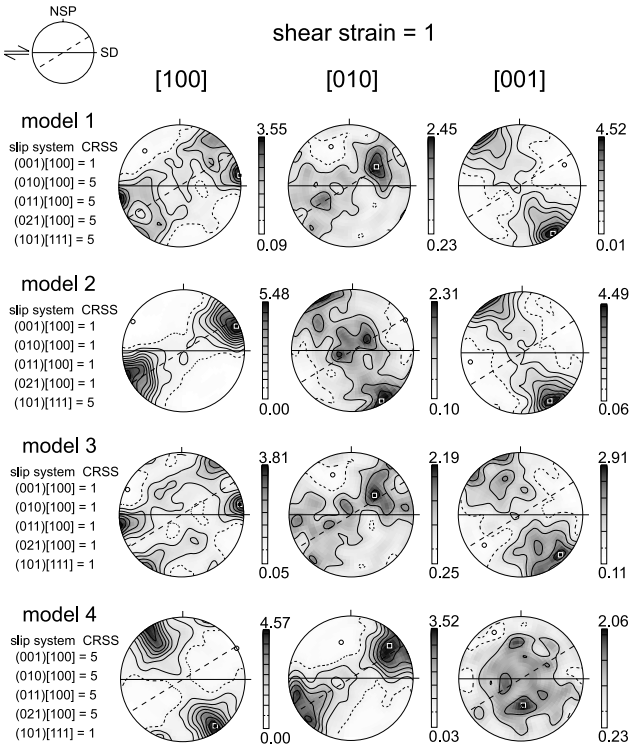

Figure 2. Wadsleyite crystal preferred orientations predicted by VPSC models. Critical resolved shear stresses (CRSS) for [100] and 1/2⟨111⟩ slip systems used in models 1 to 4 are displayed to the left of each pole figure. Projections are lower hemisphere equal-area, contours are at intervals of 0.5 multiple of a uniform distribution of 500 grains. Shear is dextral; SD, shear direction; NSP, normal to the shear plane, which is marked by the solid line. Dashed line marks the foliation (main flattening plane).

imposed dextral shear. A different pattern is only observed in model 4 that shows [100] aligned normal to the foliation (flattening plane) and [010] parallel to the lineation (main stretching direction). However, 95% of strain in this model is accommodated by glide on 1/2⟨111⟩{101} systems (Figure 3), in disagreement with frequent observations of [100] dislocations in experimentally deformed wadsleyite crystals [*Dupas et al.*, 1994; *Sharp et al.*, 1994; *Dupas-Bruzek et al.*, 1998; *Thurel et al.*, 2003b].

[13] In models 1 to 3, the [010] axes distribution is sensitive to the relative activity of [100] and ⟨111⟩ systems. In model 2, high activity of [100] systems (Figure 3) results in a girdle distribution of [010] normal to the lineation with weak maxima both normal and within the foliation. High activity of 1/2⟨111⟩{101} as observed in models 1 and 3 results, in contrast, in a girdle distribution of [010] roughly parallel to the foliation with weak maxima at ∼10–30° to the lineation. It also results in a faster reorientation of [100] toward the shear direction. Varying the CRSS and hence the activity of the different slip systems (Figure 3) also modifies the strength of the [100] and [001] maxima. High activity of [100] systems, as observed in model 2, in which these systems accommodate ∼70% of the total strain, lead to stronger concentrations of [100] relative to [001] and [010]. Similar activities of 1/2⟨111⟩ and [100] systems, as observed in models 1 and 3, results in similar concentrations for all three axes. Finally, dominant slip on 1/2⟨111⟩{101} results in very weak alignment of [001].

[14] TEM observations of similar densities of [100] and 1/2⟨111⟩ dislocations in deformed wadsleyite crystals

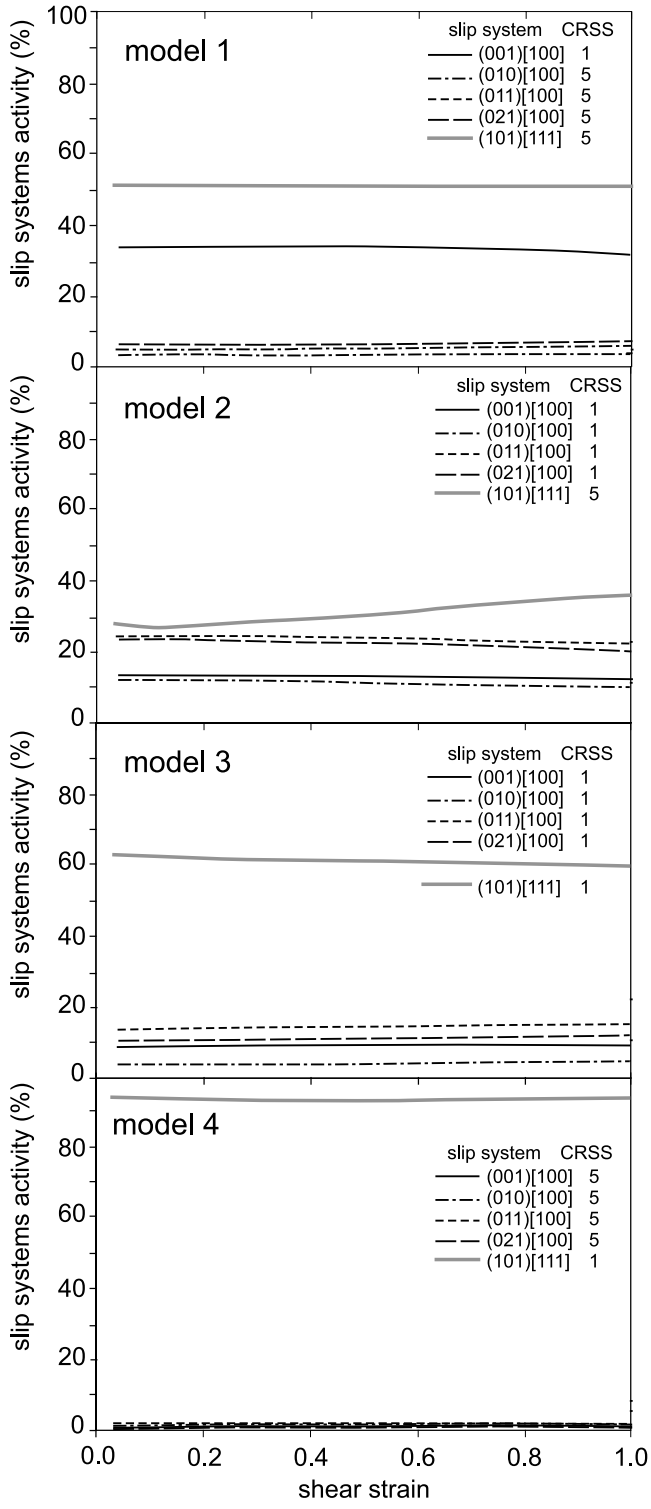

Figure 3. Slip systems activity as a function of strain in the VPSC simulations. The activity of a slip system is calculated by averaging over all grains the contribution of this slip system to the local strain rate.

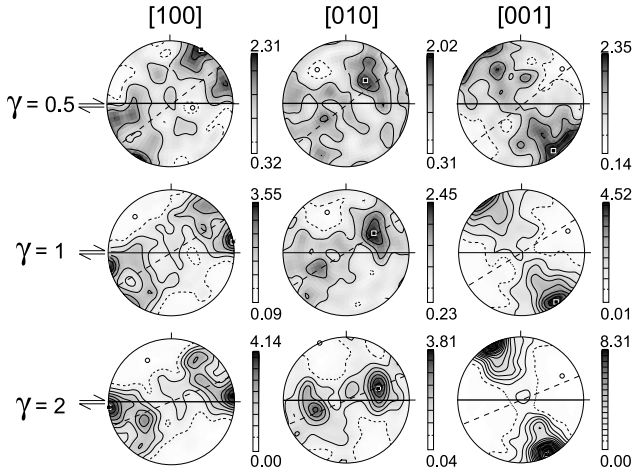

Figure 4. Wadsleyite crystal preferred orientations evolution as a function of shear strain (γ) predicted by model 1, in which slip on [100](001) is 5 times easier than slip on $1/2\langle 111\rangle\{101\}$ and on the other [100] systems. Easier slip on [100](001) at high pressure may result from the lower pressure dependence of its shear modulus relative to those of the other slip systems [*Thurel*, 2001]. Projections are lower hemisphere equal-area, contours are at intervals of 0.5 multiple of a uniform distribution of 500 grains. Dextral shear is indicated by arrows; solid line marks the shear plane, and dashed line indicates the foliation (flattening plane).

[*Thurel et al.*, 2003b] that suggest equivalent activities for [100] and $1/2\langle 111\rangle$ systems are better matched by Models 1 and 3 (Figure 3), which produce very similar CPO. Analysis of CPO development at increasing strain in these models shows that wadsleyite CPO evolves slowly with increasing strain (Figure 4). CPO obtained for a shear strain of 2 is very similar, although stronger, to the ones produced at shear strains of 0.5 and 1. [001] axes concentrate faster than [100] and [010] axes. On the other hand, the rotation of [100] axes toward the shear plane is faster than the reorientation of [001] axes toward the normal to the shear plane. Indeed, [100] axes are roughly aligned with the shear direction at a shear strain of 1, whereas (001) planes remain oblique to the shear plane even at a shear strain of 2 (Figure 4).

[15] Simulations in transtension, transpression, axial compression and axial extension show that, even for three-dimensional deformations, wadsleyite CPO patterns display stable characteristics. [100] axes tend to parallel the principal stretching direction and [001] the main shortening direction. Indeed, [100] and [001] distributions in transpression and transtension are only slightly modified relatively to those observed in simple shear. In transpression, [100] tends to form a girdle at low angle to the foliation plane. Similarly, transtension results in dispersion of [001] normal to the lineation. In addition, while transpression promotes dispersion of [010] in the foliation plane, in transtension, [010] tends to form two girdles at $\sim 50^\circ$ to the lineation.

3. Predicting Strain-Induced Seismic Anisotropy in the Upper Transition Zone

[16] The three-dimensional distribution of seismic velocities in a polycrystalline aggregate may be estimated by averaging the individual grain elastic tensors as a function of the crystallographic orientations and mineralogical composition of the aggregate [*Mainprice and Humbert*, 1994]. Seismic properties of an aggregate of pyrolitic composition under upper transition zone conditions (60% wadsleyite, 40% garnet) were estimated using elastic constants tensors of wadsleyite [*Zha et al.*, 1997; *Sinogeikin et al.*, 1998] and pyrope-rich garnet [*Chai et al.*, 1997]. Since temperature dependences of wadsleyite elastic constants are not available, seismic properties were evaluated for transition zone pressures (15–17 GPa), but ambient temperature. Yet, for most rock-forming minerals, like olivine, temperature has a strong effect on seismic velocities, but a minor influence on anisotropy [*Mainprice et al.*, 2000].

[17] Seismic properties were evaluated for wadsleyite CPO predicted by the various models. However, since the seismic properties obtained for the different models are very similar, we only present those calculated using the CPO predicted for a shear strain of 1 by model 1, which reproduces well slip systems activities inferred from TEM observations. Garnet crystals are assigned a random orientation, because observations in naturally deformed rocks and VPSC simulations show that garnet CPO is always very weak [*Mainprice et al.*, 2004]. Moreover, garnet is nearly elastically isotropic (Figure 5) and its main contribution is to reduce the rock anisotropy. Calculated elastic constants are shown in Table 1.

[18] Both compressional and shear waves display weak anisotropies ($\leq$2%, Figure 6). Compressional waves that propagate at low angle to the shear plane are faster than those traveling normal to it, the fastest velocities being observed for waves propagating at $\sim 20^\circ$ counter clockwise from the shear direction, in agreement with the imposed dextral shear. Shear wave polarization anisotropy is characterized by faster propagation of waves polarized at low angles to the shear direction and the largest delay times are observed for propagation within the shear plane at high angle to the shear direction. A nearly isotropic behavior (e.g., no shear wave splitting) should be recorded by shear waves propagating either parallel to the shear direction or normal to the shear plane. The propagation anisotropy of the fast and slow shear waves is characterized by contrasting velocity distribution patterns for the two polarizations. Shear waves polarized at low angles to the shear direction (S1) display a roughly tetragonal symmetry with a slow fourfold symmetry axis at a high angle to the shear plane, whereas those polarized normal to the shear direction (S2) show a fast fourfold symmetry axis at $\sim 20^\circ$ counter clockwise from the shear direction. Calculation of seismic properties using wadsleyite CPO predicted for different finite strains shows that anisotropy for both *P* and *S* waves evolves slowly with increasing strain (Figure 7). For a shear strain of 2, the *P* wave propagation anisotropy is 3%, the maximum *S* wave polarization anisotropy is 2.7%, and the propagation anisotropy of the fast and slow *S* waves is still lower (2.3 and 1%, respectively).

[19] It is interesting to note that, in contrast to olivine, seismic velocity and anisotropy distributions in wadsleyite polycrystals (Figure 6) do not correlate in a simple manner to the single-crystal properties (Figure 5). In the single crystal, *P* wave propagation is fastest parallel to the [010] axis and slowest parallel to [001]. The maximum *S* wave

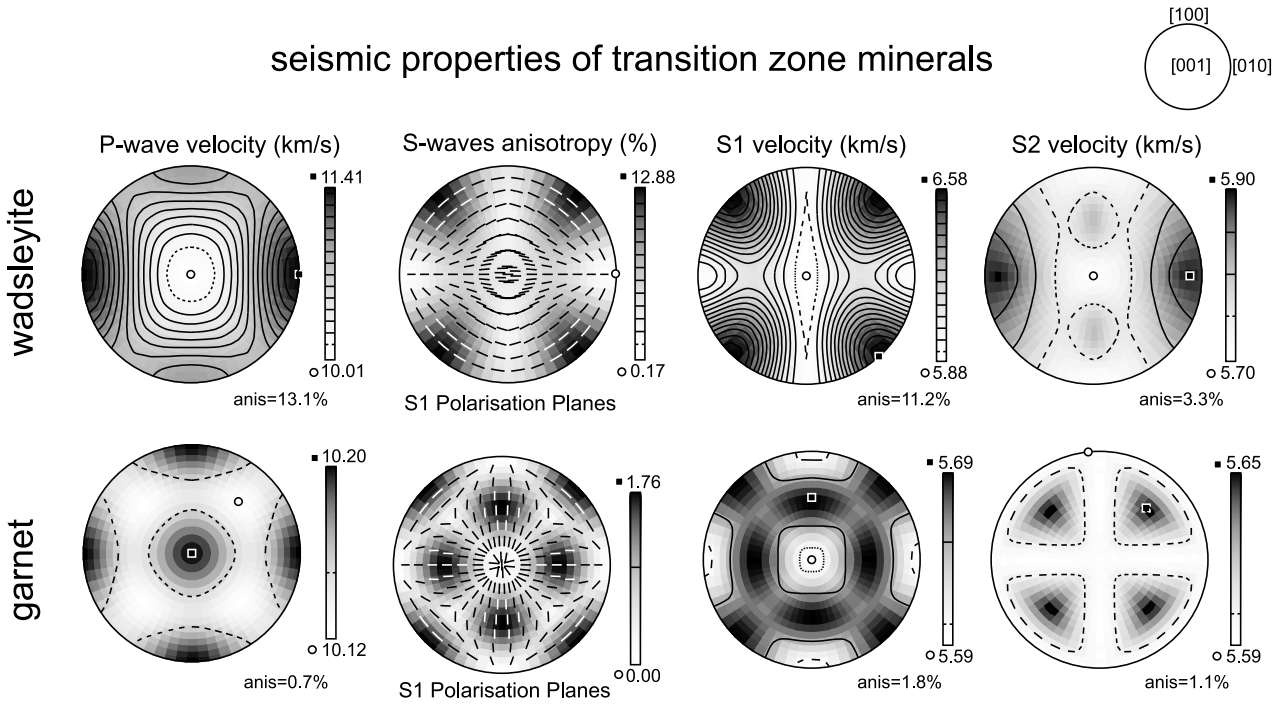

Figure 5. Seismic properties of the wadsleyite and garnet crystals at upper transition zone pressure and ambient temperature. Projections are lower hemisphere equal-area, and the crystallographic reference frame is indicated in top right inset. Contours are at intervals of 0.1 km/s for compressional waves, of 0.05 km/s for shear waves, and of 1% for shear waves polarization anisotropy.

polarization anisotropy is observed for ray paths parallel to the [110] axis, the fast *S* wave being polarized parallel to the [010] axis. In wadsleyite-rich polycrystals, the slowest *P* wave propagation is still parallel to the [001] maximum (i.e., at high angle to the shear plane), but the fastest propagation direction and the polarization of the fast *S* wave are not parallel to the [010] maximum but at low angle to the [100] maximum, i.e., at low angle to the shear direction. This seismic velocity distribution, which probably results from the dispersion of [010] axes in the polycrystals, explains why the anisotropy of wadsleyite polycrystals is relatively weak when compared to the single-crystal properties.

[20] Seismic velocity distributions calculated using wadsleyite CPO deformed in transtension or transpression are similar to those obtained for simple shear, but increasing pure shear leads to more axisymmetric patterns. Shortening normal to the shear plane results in high *P* wave velocities and *S* wave splitting within the foliation, i.e., in a low-velocity symmetry axis normal to the foliation. In contrast, extension normal to the shear plane produces low *P* wave velocities and high *S* wave splitting normal to the maximum stretching direction, i.e., in a high-velocity symmetry axis parallel to the lineation. However, the main characteristics of the seismic anisotropy pattern: fast propagation of *P* waves and polarization of the fast *S* wave at low angle to the shear direction remain unchanged.

4. Discussion: Seismic Anisotropy and Mantle Flow in the Transition Zone

[21] Viscoplastic self-consistent modeling of CPO development in wadsleyite polycrystals submitted to simple shear shows that [100] axes tend to rotate toward the shear direction and [001] axes to concentrate normal to the foliation, i.e., at high angle to the shear plane. A polycrystal of pyrolitic composition (60% wadsleyite, 40% garnet) with this CPO will show a weak seismic anisotropy at transition zone conditions. Both *P* and *S* wave anisotropy patterns show an orthorhombic symmetry. However, maximum velocities as well as polarization directions of the fast split *S* wave are rotated counterclockwise from the shear direction, paralleling the maximum stretching direction. A similar obliquity is observed in seismic properties of olivine polycrystals estimated from VPSC simulations [*Tommasi et al.*, 2000]. Analysis of olivine CPO evolution in simple shear experiments shows nevertheless that this obliquity is erased by dynamic recrystallization at shear strains >1 [*Zhang and Karato*, 1995; *Bystricky et al.*, 1999]. However, strains achieved in high-pressure deformation experiments

Table 1. Elastic Stiffness Coefficients C_{ij} Calculated for an Aggregate of Pyrolitic Composition[a]

	i					
j	1	2	3	4	5	6
1	398.96	150.96	151.03	−0.17	0.12	−3.65
2	150.96	406.32	151.60	0.05	0.20	−3.54
3	151.03	151.60	403.80	0.17	0.20	−0.70
4	−0.17	0.05	0.17	127.24	−1.88	0.27
5	0.12	0.20	0.20	−1.88	125.35	−0.21
6	−3.65	−3.54	−0.70	0.27	−0.21	125.51

[a] C_{ij} in GPa. Pyrolitic composition 60% wadsleyite, 40% garnet displaying the wadsleyite CPO shown in Figure 2 (top) at 15 GPa and ambient temperature. Reference frame 1, shear direction; 2, normal to the shear plane.

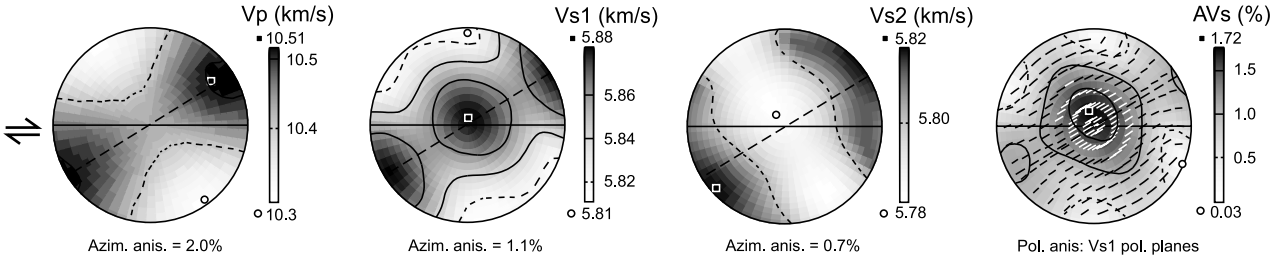

Figure 6. Modeled three-dimensional compressional and shear waves velocity distributions and shear wave polarization anisotropy (intensity and polarization direction of the fast shear wave) of a sheared aggregate of pyrolitic composition (60% wadsleyite, 40% garnet) under upper transition zone conditions. Voigt-Reuss-Hill averages are used. Projection is lower hemisphere equal-area, contours are at intervals of 0.1 km/s for compressional waves, of 0.02 km/s for shear waves, and of 0.5% for shear waves polarization anisotropy. Solid and dashed lines mark the shear plane and the foliation, respectively. Arrows indicate the shear sense (dextral). Elastic constants for this model are presented in Table 1.

on wadsleyite polycrystals are still too low to produce dynamic recrystallization, making any inference on the effect of this process on wadsleyite CPO evolution highly speculative.

[22] Analysis of seismological observations of anisotropy in the transition zone in the light of the present model results may constrain the geometry of flow in the upper transition zone. Indeed, only horizontal shearing results in faster velocities both for horizontally propagating compressional waves (*PH*) and for horizontally polarized shear waves (*SH*) as observed by [*Montagner and Kennett*, 1996; *Beghein and Trampert*, 2004]. Analysis of Figure 8a shows that horizontal shearing also produces azimuthal anisotropy patterns for horizontally propagating *S* waves similar to those inferred from Love wave overtone data [*Trampert and van Heijst*, 2002]: anisotropy for vertically polarized shear waves (*SV*) is twice as strong as the one observed for horizontally polarized shear waves (*SH*). Moreover, *SV* and *SH* velocity variations display 180° and 90° periodicities, respectively, in good agreement with the observed 2ψ and 4ψ dependences for *SV* and *SH* azimuthal anisotropy, respectively [*Trampert and van Heijst*, 2002]. Inclination of the shear plane ($\leq$25°) from horizontal does not modify significantly the *S* wave azimuthal anisotropy pattern (Figure 8a). On the other hand, shearing on steeply dipping planes induces opposite periodicities for *SV* and *SH* velocity variations (Figure 8b). Modeled anisotropy amplitudes (<1% for *SV*) are significantly weaker than those inferred from Love wave overtone data (up to 2%). However, amplitudes are poorly constrained in these inversions [*Trampert and van Heijst*, 2002], hindering an interpretation of this misfit in terms of higher strain or of an additional contribution to the measured seismic anisotropy.

[23] A horizontally sheared upper transition zone would be seen as an isotropic medium by vertically propagating shear waves, such as *SKS*. In contrast, horizontally propagating *S* waves will be split with *SH* faster than *SV*, in agreement with observations using *S* waves turning in the transition zone beneath northern Australia and within the northern Tonga subduction zone [*Tong et al.*, 1994; *Chen and Brudzinski*, 2003]. Both data sets show horizontally polarized shear waves (*SH*) arriving 2–3 s earlier than vertically polarized shear waves (*SV*). These delay times may be explained by 1–1.5% anisotropy in the upper transition zone [*Chen and Brudzinski*, 2003], in good agreement with model predictions of 0.7 to 1.7% polarization anisotropy for *S* wave propagating parallel to the shear plane.

[24] On the other hand, steeply dipping flow in the vicinity of tectonically active regions may explain observations that point to faster propagation of *PV* [*Beghein and Trampert*, 2004] or to a weak contribution of the transition zone to *SKS* splitting near the South Kurils subduction [*Fouch and Fischer*, 1996]. However, even in this case, the maximum delay time that a vertically traveling shear wave may accumulate in its 100 km long path in the upper transition zone is roughly 0.2 s. This value is at the resolution level for *SKS* and *SKKS* splitting data, probably explaining why studies using these phases find little evidence for anisotropy in the transition zone.

[25] Seismological observations of anisotropy in the transition zone may therefore be explained by wadsleyite CPO

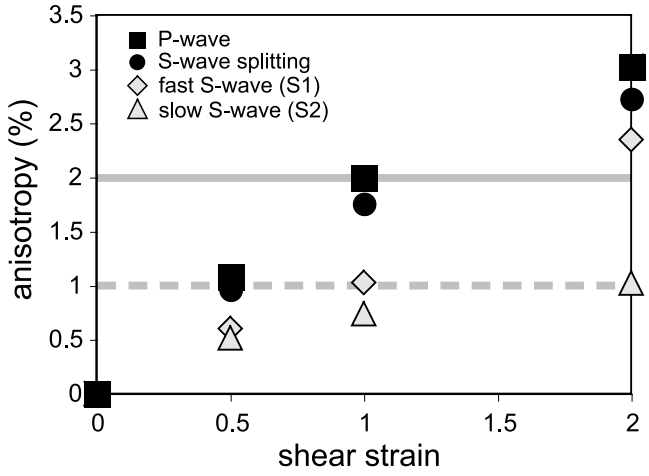

Figure 7. Evolution of seismic anisotropy as a function of finite strain. Squares mark compressional waves propagation anisotropy, circles mark the maximum shear wave polarization anisotropy, and gray diamonds and triangles mark propagation anisotropies for the fast and slow shear wave, respectively. For comparison, maximum amplitude of azimuthal anisotropy of *SV* and *SH* (solid and dashed gray lines, respectively) in the transition zone inferred from Love wave overtone data [*Trampert and van Heijst*, 2002] is also displayed.

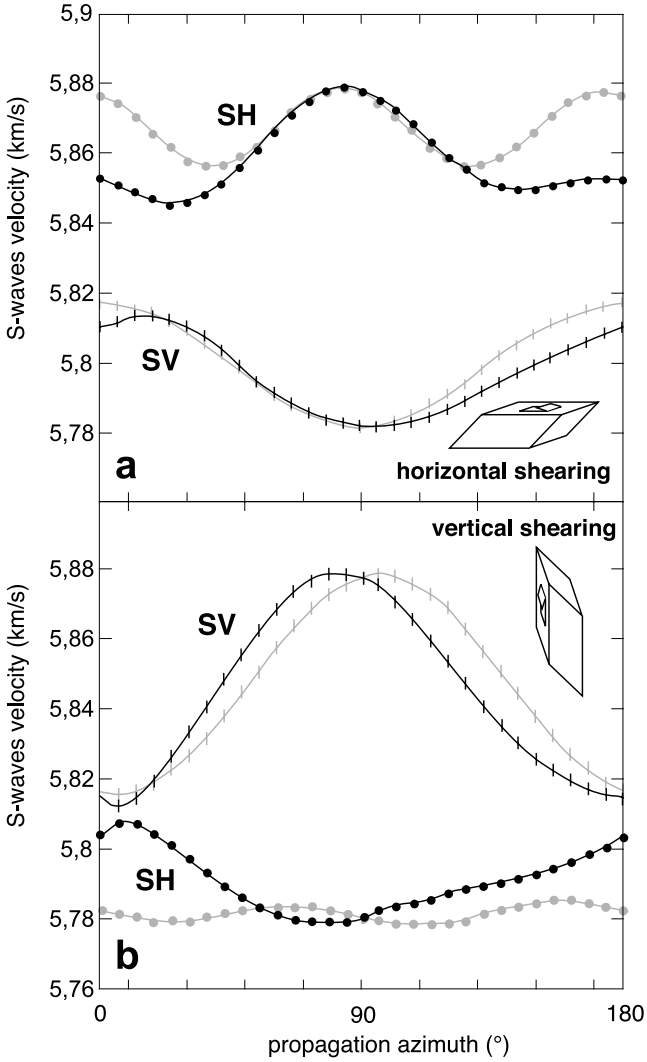

Figure 8. Modeled azimuthal anisotropy for horizontally propagating shear waves in the upper transition zone, considering (a) horizontal shearing and (b) vertical shearing. Azimuthal velocity variations for shallow (25°) (Figure 8a) and steeply dipping (65°) (Figure 8b) shear planes are also displayed (gray lines).

produced by dominant horizontal shear in the transition zone, steeply dipping flow across the transition zone being limited to the vicinity of tectonically active regions. Dominant horizontal shearing in the transition zone suggests that this layer acts as a boundary layer in the mantle convection system. The flow pattern inferred from seismic anisotropy data using our model predictions is therefore in good agreement with seismic tomography data [*Gorbatov and Kennett*, 2003] and convection models [*Machetel and Weber*, 1991; *Brunet and Machetel*, 1998; *Brunet and Yuen*, 2000] that show that phase changes in the transition zone hamper material across the transition zone.

[26] To further constrain the effect of phase changes on the transition zone flow pattern, we compare tangential and radial flow in spherical mantle circulation models that compute the present-day mantle convective flow driven both by plate motions and the internal density anomaly distribution observed in global tomographic models [*Thoraval et al.*, 1995]. Two models are considered: (1) a model with only a viscosity increase at 670 km depth and (2) a model with the same viscosity and phase changes at the top and bottom of the transition zone. Phase change locations depend on the local temperature and pressure through the Clapeyron slopes. The kinetics of the reactions, which may lead to persistence of metastable phases, is introduced as a delay time to phase change to occur [*Thoraval and Machetel*, 2000]. Analysis of the tangential to radial velocity ratios at various depths in these models shows that allowing for phase changes at 410 and 670 km strongly enhances tangential flow in the transition zone (Figure 9). Average tangential (horizontal) velocities are two to three times higher than radial (vertical) ones in the upper transition zone. An independent constraint on these results is that the model with self-consistent phase changes retrieves both the observed geoid and low-amplitude dynamic topography, while the model with solely a viscosity jump predicts anomalously high dynamic topography.

5. Conclusion

[27] Forward models based on recent high-pressure experimental data on mantle minerals show that plastic deformation of wadsleyite may result in weak seismic

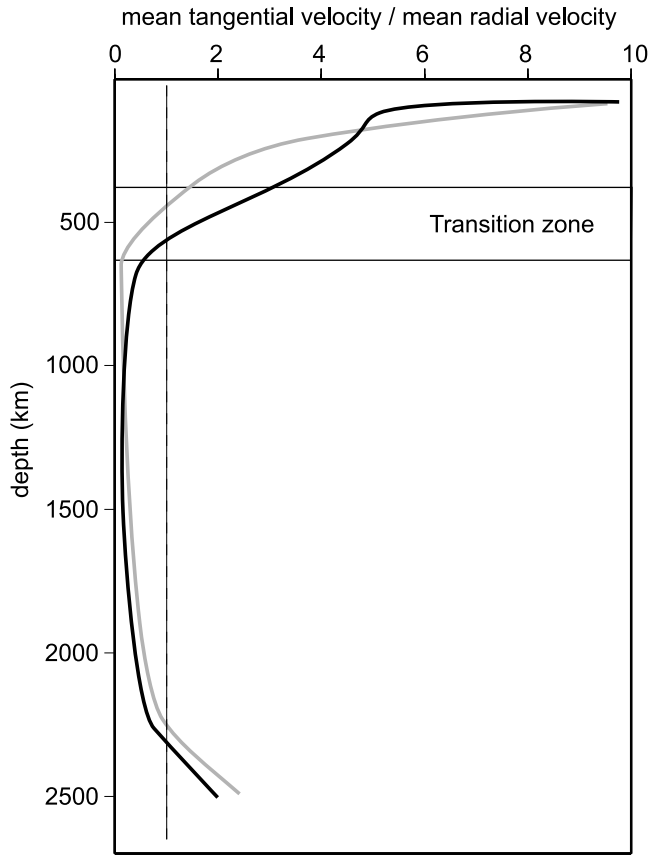

Figure 9. Ratio of RMS amplitudes of tangential and radial velocities as a function of depth in mantle circulation models [*Thoraval and Machetel*, 2000] with (black line) and without (gray line) phase changes at the top and at the base of the transition zone. Dashed line marks equal amplitudes of tangential and radial velocities.

anisotropy in the upper transition zone. *P* waves propagate faster at low angle to the shear direction and slower at high angle to the shear plane. *S* wave anisotropy is characterized by faster propagation of waves polarized subparallel to the shear direction. The azimuthal anisotropy of two *S* wave polarizations depends strongly on the propagation direction. Horizontal shearing results therefore in higher velocities for horizontally propagating *P* waves (*PH*) and horizontally polarized *S* waves (*SH*), as well as in weak azimuthal variation of *SV* and *SH* velocity, characterized by faster propagation of *SV* and *SH* parallel and normal to the flow direction, respectively. On the other hand, vertical flow leads to higher velocities for vertically propagating *P* waves (*PV*) and vertically polarized *S* waves (*SV*) and to a weak azimuthal variation of *SV* velocity with the fastest propagation normal to the shear plane. Although these models only consider deformation by dislocation glide and simple flow patterns, they may explain seismological observations of anisotropy in the transition zone if this layer deforms dominantly by horizontal shear, with steeply dipping flow limited to the vicinity of tectonically active regions. Such a flow pattern is coherent with seismic tomography data and geodynamic models that show that phase changes in the transition zone hamper, but do not completely block material transfer across the transition zone. Convergence between flow patterns inferred using independent methods suggests that the present models provide good constraints on the relation between deformation and anisotropy in the upper transition zone. Further developments on high-pressure experimental techniques will allow to test these predictions and to assess the effect of other deformation mechanisms like dynamic recrystallization on the wadsleyite CPO evolution and hence on the seismic anisotropy patterns in the transition zone.

[28] **Acknowledgments.** This work would not exist without G. Canova, who introduced A.T. and D.M. to VPSC modeling. R. Lebensohn is thanked for access to the VPSC code, and J. Trampert is thanked for helpful discussions on observations of seismic anisotropy in the transition zone.

References

Akaogi, M., E. Ito, and A. Navrotsky (1989), Olivine-modified spinel-spinel transitions in the system Mg_2SiO_4-$FeSiO_4$: Calorimetric measurements, thermomechanical calculation, and geophysical interpretation, *J. Geophys. Res.*, *94*, 15,671–15,685.

Bascou, J., A. Tommasi, and D. Mainprice (2002), Plastic deformation and development of clinopyroxene lattice preferred orientations in eclogites, *J. Struct. Geol.*, *24*, 1357–1368.

Beghein, C., and J. Trampert (2004), Probability density functions for radial anisotropy: Implications for the upper 1200 km of the mantle, *Earth Planet. Sci. Lett.*, *217*, 151–162.

Blackman, D. K., J.-M. Kendall, P. R. Dawson, H.-R. Wenk, D. Boyce, and J. Phipps-Morgan (1996), Teleseismic imaging of subaxial flow at mid-ocean ridges: Travel-time effects of anisotropic mineral texture in the mantle, *Geophys. J. Int.*, *127*, 415–426.

Brunet, D., and P. Machetel (1998), Large-scale tectonic features induced by mantle avalanches with phase, temperature, and pressure lateral variations of viscosity, *J. Geophys. Res.*, *103*, 4929–4945.

Brunet, D., and D. A. Yuen (2000), Mantle plumes pinched in the transition zone, *Earth Planet. Sci. Lett.*, *178*, 13–27.

Bussod, B. Y., T. Katsura, and D. C. Rubie (1993), The large volume multi-anvil press as a high P-T deformation apparatus, *Pure Appl. Geophys.*, *141*, 1–20.

Bystricky, M., L. Burlini, K. Kunze, and J. P. Burg (1999), Experimental deformation of olivine aggregates to high strains in torsion, *Göttinger Arb. Geol. Paläontol.*, *4*, 22–23.

Cadek, O., and L. Fleitout (1999), A global geoid model with imposed plate velocities and partial layering, *J. Geophys. Res.*, *104*, 29,055–29,075.

Chai, M., J. M. Brown, and L. J. Slutsky (1997), The elastic constants of a pyrope-grossular-almandine garnet up to 20 GPa, *Geophys. Res. Lett.*, *24*, 523–526.

Chastel, Y. B., P. R. Dawson, H.-R. Wenk, and K. Bennet (1993), Anisotropic convection with implications for the upper mantle, *J. Geophys. Res.*, *98*, 17,757–17,771.

Chen, W.-P., and M. R. Brudzinski (2003), Seismic anisotropy in the mantle transition zone beneath Fiji-Tonga, *Geophys. Res. Lett.*, *30*(13), 1682, doi:10.1029/2002GL016330.

Christensen, U. R., and D. A. Yuen (1985), Layered convection induced by phase transitions, *J. Geophys. Res.*, *90*, 10,291–10,300.

Cordier, P., and D. C. Rubie (2001), Plastic deformation of minerals under extreme pressure using a multi-anvil apparatus, *Mater. Sci. Eng. A*, *309–310*, 38–43.

Dupas, C., N. Doukhan, J. C. Doukhan, H. W. Green II, and T. E. Young (1994), Analytical electron microscopy of a synthetic peridotite experimentally deformed in the beta-olivine stability field, *J. Geophys. Res.*, *99*, 15,821–15,832.

Dupas-Bruzek, C., T. G. Sharp, D. C. Rubie, and W. B. Durham (1998), Mechanisms of transformation and deformation in $Mg_{1.8}Fe_{0.2}SiO_4$ olivine and wadsleyite under non-hydrostatic stress, *Phys. Earth Planet. Inter.*, *108*, 33–48.

Durham, W. B., D. J. Weidner, S.-I. Karato, and Y. Wang (2002), New developments in deformation experiments at high pressure, in *Plastic Deformation of Minerals and Rocks*, *Rev. Mineral. Geochem.*, vol. 51, edited by S.-I. Karato and H.-R. Wenk, pp. 21–49, Am. Mineral. Soc., Washington, D. C.

Fouch, M. J., and K. M. Fischer (1996), Mantle anisotropy beneath northwest Pacific subduction zones, *J. Geophys. Res.*, *101*, 15,987–16,002.

Gorbatov, A., and B. L. N. Kennett (2003), Joint bulk-sound and shear tomography for western Pacific subduction zones, *Earth Planet. Sci. Lett.*, *210*, 527–543.

Kaminski, E., and N. M. Ribe (2002), Timescales for the evolution of seismic anisotropy in mantle flow, *Geochem Geophys. Geosyst.*, *3*(8), 1015, doi:10.1029/2001GC000222.

Lebensohn, R. A., and C. N. Tomé (1993), A self-consistent anisotropic approach for the simulation of plastic deformation and texture development of polycrystals: Application to zirconion alloys, *Acta Metall. Mater.*, *41*, 2611–2624.

Lebensohn, R. A., P. R. Dawson, H. M. Kern, and H.-R. Wenk (2003), Heterogeneous deformation and texture development in halite polycrystals: Comparison of different modeling approaches and experimental data, *Tectonophysics*, *370*, 287–311.

Logé, R. E., J. W. Signorelli, Y. B. Chastel, M. Y. Perrin, and R. A. Lebensohn (2000), Sensitivity of alpha-Zy4 high-temperature deformation textures to the beta-quenched precipitate structure and to recrystallization: Application to hot extrusion, *Acta Mater.*, *48*, 3917–3930.

Machetel, P., and P. Weber (1991), Intermittent layered convection in a model mantle with an endothermic phase change at 670 km, *Nature*, *350*, 55–57.

Mainprice, D., and M. Humbert (1994), Methods of calculating petrophysical properties from lattice preferred orientation data, *Surv. Geophys.*, *15*, 575–592.

Mainprice, D., G. Barruol, and W. Ben Ismaïl (2000), The seismic anisotropy of the Earth's mantle: From single crystal to polycrystal, in *Earth's Deep Interior: Mineral Physics and Seismic Tomography From Atomic to Global Scale*, *Geophys. Monogr. Ser.*, vol. 117, edited by S.-I. Karato et al., pp. 237–264, AGU, Washington, D. C.

Mainprice, D., J. Bascou, P. Cordier, and A. Tommasi (2004), Crystal preferred orientations of garnet: Comparison between numerical simulations and electron back-scattered diffraction (EBSD) measurements in naturally deformed eclogites, *J. Struct. Geol.*, *26*, 2089–2102.

Molinari, A., G. R. Canova, and S. Azhy (1987), A self-consistent approach of the large deformation polycrystal viscoplasticity, *Acta Metall.*, *35*, 2983–2994.

Montagner, J.-P., and B. L. N. Kennett (1996), How to reconcile body-wave and normal-mode reference earth models, *Geophys. J. Int.*, *125*, 229–248.

Ribe, N. M. (1989), Seismic anisotropy and mantle flow, *J. Geophys. Res.*, *94*, 4213–4223.

Sachs, G. (1928), Zur ableitung einer fliessbedingung, *Z. Ver. Dtsch. Ing.*, *72*, 734–736.

Sharp, T. G., B. Y. Bussod, and T. Katsura (1994), Microstructures in β-$Mg_{1.8}Fe_{0.2}SiO_4$ experimentally-deformed at transition zone conditions, *Phys. Earth Planet. Inter.*, *86*, 69–83.

Sinogeikin, S. V., T. Katsura, and J. D. Bass (1998), Sound velocities and elastic properties of Fe-bearing wadsleyite and ringwoodite, *J. Geophys. Res.*, *103*, 20,819–20,825.

Taylor, G. I. (1938), Plastic strain in metals, *J. Inst. Metals*, *62*, 301–324.

Thoraval, C., and P. Machetel (2000), Accounting for phase changes and their kinetics within geodynamic models for the geoid, *Eos Trans. AGU*, *81*(48), Fall Meet. Suppl., Abstract T22E-07.

Thoraval, C., P. Machetel, and A. Cazenave (1995), Locally layered convection inferred from dynamic models of the Earth's mantle, *Nature*, *375*, 777–780.

Thurel, E. (2001), Etude par microscopie electronique en transmission das mécanismes de déformation de la wadsleyite et de la ringwoodite, Ph.D. thesis, Univ. des Sci. et Technol., Lille, France.

Thurel, E., and P. Cordier (2003), Plastic deformation of wadsleyite: I. High-pressure deformation in compression, *Phys. Chem. Miner.*, *30*, 256–266.

Thurel, E., P. Cordier, D. Frost, and S.-I. Karato (2003a), Plastic deformation of wadsleyite: II. High-pressure deformation in shear, *Phys. Chem. Miner.*, *30*, 267–270.

Thurel, E., J. Douin, and P. Cordier (2003b), Plastic deformation of wadsleyite: III. Interpretation of dislocations and slip systems, *Phys. Chem. Miner.*, *30*, 271–279.

Tomé, C. N., H.-R. Wenk, G. R. Canova, and U. F. Kocks (1991), Simulations of texture development in calcite: Comparison of polycrystals plasticity theories, *J. Geophys. Res.*, *96*, 11,865–11,875.

Tommasi, A. (1998), Forward modeling of the development of seismic anisotropy in the upper mantle, *Earth Planet. Sci. Lett.*, *160*, 1–13.

Tommasi, A., B. Tikoff, and A. Vauchez (1999), Upper mantle tectonics: Three-dimensional deformation, olivine crystallographic fabrics and seismic properties, *Earth Planet. Sci. Lett.*, *168*, 173–186.

Tommasi, A., D. Mainprice, G. Canova, and Y. Chastel (2000), Viscoplastic self-consistent and equilibrium-based modeling of olivine lattice preferred orientations. Implications for upper mantle seismic anisotropy, *J. Geophys. Res.*, *105*, 7893–7908.

Tong, C., O. Gudmundsson, and B. L. N. Kennett (1994), Shear wave splitting in refracted waves returned from the upper mantle transition zone beneath northern Australia, *J. Geophys. Res.*, *99*, 15,783–15,797.

Trampert, J., and H. J. van Heijst (2002), Global azimuthal anisotropy in the transition zone, *Science*, *296*, 1297–1299.

van der Hilst, R. D., R. Engdahl, W. Spakman, and G. Nolet (1991), Tomographic imaging of subducted lithosphere below Northwest Pacific island arcs, *Nature*, *353*, 37–43.

Vinnik, L. P., and J. P. Montagner (1996), Shear wave splitting in the mantle *Ps* phases, *Geophys. Res. Lett.*, *23*, 2449–2452.

Wenk, H.-R., K. Bennet, G. R. Canova, and A. Molinari (1991), Modelling plastic deformation of peridotite with the self-consistent theory, *J. Geophys. Res.*, *96*, 8337–8349.

Zha, C. S., T. S. Duffy, H. Mao, R. T. Downs, R. J. Hemley, and D. J. Weidner (1997), Single-crystal elasticity of β-Mg_2SiO_4 to the pressure of the 410 km seismic discontinuity in the Earth's mantle, *Earth Planet. Sci. Lett.*, *147*, E9–E15.

Zhang, S., and S. Karato (1995), Lattice preferred orientation of olivine aggregates in simple shear, *Nature*, *375*, 774–777.

P. Cordier, Laboratoire Structure et Propriétés de l'Etat Solide, CNRS/Université de Lille, F-59650 Villeneuve d'Ascq cedex, France.

H. Couvy, Bayerisches Geoinstitut, Universität Bayreuth, D-95440 Bayreuth, Germany.

D. Mainprice, C. Thoraval, and A. Tommasi, Laboratoire de Tectonophysique, CNRS/Université de Montpellier II, F-34095 Montpellier cedex 5, France. (deia@dstu.univ-montp2.fr)